Potential of NMR relaxometry to unravel the properties of mucilage in several pore sizes

Mathilde Brax[a], Maximilian Köhne[b], Eva Kroener[c], Gabriele Ellen Schaumann[a*]

[a] University Koblenz-Landau, Institute for Environmental Sciences, Group of Environmental and Soil Chemistry, Fortstrasse 7, 76829 Landau, Germany.

[b] Helmholtz Centre for Environmental Research GmbH – UFZ, Department of Soil System Sciences, Theodor-Lieser-Strasse 4, 06120 Halle, Germany.

[c] University Koblenz-Landau, Institute for Environmental Sciences, Geophysics, Fortstrasse 7, 76829 Landau, Germany

*schaumann@uni-landau.de, +49 6341 280 31571

Keywords

Mucilage, pore size, ^{1}H NMR relaxometry, gel effect, water mobility

Abstract

Soil-born exudates such as mucilage are known to affect soil physicochemical properties. Characterization of the gel properties of mucilage at the pore-scale is necessary to gain mechanistic understanding of the underlying processes leading to changes of soil properties. Yet, mucilage intrinsic properties´ complicate its *in-situ* detection. Longitudinal and transverse magnetic relaxation rates measured with ^{1}H Nuclear Magnetic Resonance (NMR) relaxometry have the potential to study mucilage-water interactions *in-situ* as they are sensitive to restricted molecular motion of water protons in biohydrogels. However, the relations between water mobility and biohydrogel properties in porous media have remained unknown until now.

In this study, the mobility of water molecules in chia seed mucilage in porous systems was systematically investigated by means of ^{1}H-NMR relaxometry. Chia seed mucilage was used as it has hydrogel properties shared by a range of biological hydrogels found in soil. Glass beads of several sizes were used to study the influence of the pore size on the NMR signal.

A conceptual model based on the equations describing the relaxation of water protons in porous media was developed to integrate these gel effects into the NMR parameters. The increased rigidity of the polymer network and its organization in the pore space, which depended on the particle size and the mucilage concentration, were assessed as the gel effects significantly affecting the bulk relaxation. Our approach, which combines the use of NMR along with other imaging methods, is a promising strategy to detect and characterize the properties of biohydrogel in porous media.

1. Introduction

Due to its gel-specific properties, mucilage can modulate several soil physicochemical properties, such as soil water holding capacity or soil hydraulic conductivity (Ahmed et al., 2014; Carminati et al., 2011). Gels are characterized by high water contents, swelling and shrinking induced by moisture dynamics and viscoelastic properties (Brax et al., 2017; Capitani et al., 2015). The complexity of biohydrogel-soil interactions requires the understanding of simple systems, and coarse sand has been mostly used as artificial soil (Ahmed et al., 2014; Carminati, 2012; Gregory, 2006; Kroener et al., 2014; Zarebanadkouki et al., 2012). Recent studies showed that the particle size plays a role in the extent to which soil-water-mucilage interactions affect the percolation threshold or the stability of aggregates (Ahmed et al., 2016; Albalasmeh and Ghezzehei, 2014; Kroener et al., 2018). To elucidate the pore-scale processes, which are at the origin of changes of soil macroscopic properties, *in-situ* studies focusing on the properties of mucilage at the pore scale are necessary (Albalasmeh and Ghezzehei, 2014; Brax et al., 2017).

Recent advances in imaging techniques enable one to visualize the physical environment around the roots (Helliwell et al., 2013). Low-attenuation contrasts between water and biohydrogels make it difficult to image mucilage in porous systems with magnetic resonance imaging (MRI), X-ray computed microtomography (µCT) or neutron imaging (Brax et al., 2017). The addition of contrasting agents in biohydrogels is a method to overcome this limit (Davit et al., 2011), but still stays invasive. ^{1}H NMR relaxometry is emerging as a suitable method to differentiate mucilage from water in porous media, as biohydrogels reduce the transverse and longitudinal relaxation time of proximal water protons (Bayer et al., 2010; Brax et al., 2017; Brownstein and Tarr, 1979; Codd et al., 2011).

The asset and at the same time the difficulty of ^{1}H NMR relaxometry in porous systems come from the multitude of factors affecting the relaxation time, such as pore size, swelling of soil particles or paramagnetic inhomogeneity (Bayer et al., 2010). What is more, biohydrogels can change soil pore connectivity or effective pore size (Jaeger et al., 2006; Todoruk et al.,

2003). Therefore, characterization of biohydrogels in porous systems first necessitates the use of simple model systems, such as glass beads or sandstone, in which the gel is homogeneously distributed (Brax et al., 2018; Sanderlin et al., 2013). Until now, most ^{1}H NMR relaxometry studies on biohydrogels in porous media have focused on biofilms, although some studies have been published about synthetic hydrogels in porous media (Buchmann et al., 2015; Buchmann and Schaumann, 2016).

NMR studies on the transverse relaxation of ^{1}H spins of water in porous media (Fig. 1a) typically focused on the influence of the surface relaxivity and of the diffusion gradients on the overall relaxation behavior of the medium (see supporting information for definition) (Godefroy et al., 2001; Kleinberg et al., 1994). However, the presence of biohydrogels in the pore space changes the fingerprint of the bulk relaxation, which must be taken into consideration in this case (Fig. 1a-b) (Kirkland et al., 2015). Biofilm growth within the pore space enhanced the weighted average of bound and free protons and shifted the relaxation to shorter times (Codd et al., 2011; Jaeger et al., 2010). Most studies on the influence of biofilms in porous media measured the transverse relaxation time (T_2) with one or two-dimensional experiments (Bayer et al., 2010; Codd et al., 2011; Sanderlin et al., 2013). Until now, longitudinal relaxation (T_1) distributions of biohydrogels in soil have not been much investigated, though Bayer et al. (2010) suggested helpfully the combination of T_1 and T_2 to discriminate between the effects of water mobility and the ones of pore size distribution in biohydrogel-containing porous media. In alginate, cellulose derivate or mucilage, T_2 decreased actually stronger than T_1 due to a reduced rotational mobility of the water protons in the hydrogel (Brax et al., 2018; Degrassi et al., 1998; Fyfe and Blazek 1997).

(Figure 1)

In biohydrogel-containing porous media, water is entrapped in a hierarchical porous structure consisting of the polymer network, itself surrounded by the pore walls (Fig. 1b). As each biohydrogel has its own relaxation time fingerprint (Hills, 1992), it is necessary to characterize the relaxation of water protons in the biohydrogel in order to better assess the

biohydrogel-induced shift of the relaxation time in porous media. The mucilage concentration range in the rhizosphere was estimated to vary between 0.1 and 1.0 wt% (Carminati and Vetterlein, 2013). In this range, the longitudinal relaxation rate (R_1) ($1/T_{1\ Muc}$) and the transverse relaxation rate (R_2) ($1/T_{2\ Muc}$) of *free* chia seed mucilage varied linearly with the mucilage concentration multiplied by a factor, which we will call $G^*_{1,2\ B}$ (Brax et al., 2018).

$$\frac{1}{T_{1,2\ Muc}} = \frac{1}{T_{1,2\ BW}} + G^*_{1,2\ B} \cdot c_{Muc} \quad (1)$$

The subscript 1,2 refers to R_1 and to R_2 respectively, the subscript *BW* stands for bulk water and the subscript *B* on the *G* factor indicates that mucilage is in the bulk phase. R_2 was reported to depend stronger on the mucilage concentration than R_1, as $G^*_{2\ B}$ (0.41±0.02 wt%$^{-1}$·s^{-1}) was higher than $G^*_{1\ B}$ (0.10±0.02 wt%$^{-1}$·s^{-1}) (Brax et al., 2018). The *polymeric network effect* $G^*_{1,2\ B}$ is defined as the dependence of the relaxation rate on the mucilage concentration. In the preliminary work to this study, Brax et al. (2018) studied the proton relaxation in glass beads of several sizes mixed with water and with chia seed mucilage at one mucilage concentration of 0.5 wt% (corresponding to 500 mg dry mucilage in 100 g water). The water content in the glass beads mixed with mucilage (GB-mucilage) was set the same as in the water-saturated samples (GB-water). It was shown that the influence of mucilage on the relaxation rate, also called “gel effect”, could be quantified by using the equations describing the relaxation of water protons in a porous medium. The gel effect expressed itself by an accelerated bulk relaxation and an accelerated surface relaxation (Fig. 1b) (Brax et al., 2018).

Still, it is not clear how strong these two gel effects vary with the mucilage concentration, and how relevant they are to describe mucilage at the pore scale. Our aim was to further quantify the gel effect on the NMR parameters, in order to be finally able to describe the way gel affects the molecular mobility of water in porous media. This would help us to deduce how the water mobility reflects the gel properties in porous media. Therefore, we measured R_2 and R_1 of GB-mucilage for mucilage concentrations between 0.1 and 1.0 wt%. Mucilage was mixed with glass beads of various sizes. Our approach was double-sided: on one hand, we

hypothesized that the mucilage concentration influenced quantitatively and proportionally the NMR parameters. For this, we modified the equations describing the relaxation of water protons in the pore space under the assumption of a fast-diffusion regime (see below) and developed a conceptual model incorporating the gel effects identified by Brax et al. (2018) (Equation 6). On the other hand, we also hypothesized that the mucilage polymer network organized differently according to the pore size and expected the NMR gel effect parameters to reflect this difference.

2. Theory and conceptual model

2.1. Relaxation in porous systems

In porous systems and under the assumption of a fast-diffusion regime, R_1 and R_2 are determined by the bulk relaxation rate ($1/T_B$) and by the surface relaxation rate ($1/T_S$), and $1/T_S$ is defined by the surface relaxivity (ρ) and the surface-to-volume ratio (S/V) (Fig. 1a) (Brownstein and Tarr, 1979; Godefroy et al., 2001). In a fast-diffusion regime, water molecules can transit the pore several times before their relaxation and the magnetization decay is spatially uniform. The diffusion relaxation rate $1/T_{2D}$ originates from molecular diffusion in internal magnetic field gradients and additionally affects R_2, but not R_1 as no energy exchange is involved (Brownstein and Tarr, 1979). Internal field gradients are negligible at small echo time t_E and small magnetic field strengths (Dunn et al., 2002).

$$\frac{1}{T_{1,2\,WP}} = \frac{1}{T_{1,2B/WP}} + \frac{1}{T_{1,2S/WP}}\left(+\frac{1}{T_{2D}}\right) \tag{2}$$

The subscript *WP* refers to a porous media filled with water. The surface relaxivity describes the efficiency of the particle surface to enhance longitudinal or transverse relaxation (Brownstein and Tarr, 1979). The surface to volume ratio is a measure of the pore size and is directly connected to the diameter of the particles (D_{GB}) with the constant β for simple shapes (Equation 3) (Kleinberg, 1996).

$$\frac{1}{T_{1,2S/WP}} = \rho \cdot \frac{S}{V} = \rho \cdot \frac{\beta}{D_{GB}} \tag{3}$$

Low-field NMR has proven to be better adapted to the detection of biofilm in porous media than high-field NMR: the high susceptibility gradients inherent to high-field NMR dominate the T_2 distribution and prevent the detection of biofilm in porous media with strong susceptibility gradients (Codd et al., 2011; Sanderlin et al., 2013).

2.2. Relaxation in biohydrogels

The surface in biohydrogel corresponds to the polymer junction zones and cross-links (Belton et al., 1988; Chui et al., 1995). Surface relaxation is the predominant factor controlling the relaxation of water protons in hydrogels, and proton chemical exchange between the water protons and the exchangeable protons of the polymer is the most important surface relaxation mechanism (Li et al., 1999). There is a rapid exchange between the water molecules tumbling freely and the ones “chemisorbed” to the polysaccharide surface, and the measured relaxation time is weighted by the relaxation times of these two proton pools (Belton et al., 1988; Lüsse and Arnold, 1998). The transverse or spin-spin relaxation differs from the longitudinal or spin-lattice relaxation as it depends on direct interactions between the spins without energy transfer to the lattice. As it is mainly affected by the rotational correlation of the water molecules, the spin-spin relaxation monitors the conformation and mobility of the polysaccharide. The mobility of water molecules in direct vicinity to the polymer backbone is affected by reorientation processes of these water molecules, with respect to their physicochemical interactions with the polymer and to the mobility of the polymer backbone (Lüsse and Arnold, 1998). Thus, the relaxation behavior of water molecules in biohydrogels is expected to change from polymer to polymer due to different polymer mobility and water binding properties (Shapiro, 2011).

2.3. Conceptual model describing the gel effect on the NMR parameters

In a porous system, in which gel is homogeneously mixed with the particles, the gel fills the pores and covers the surface (Fig. 1b). If the gel polymer network within the pore has the same three-dimensional (3D) organization as the *free* gel polymer network, the bulk relaxation rate measured for the gel in porous media ($1/T_{1,2\ B/GP}$) should be equal to the

relaxation rate of the pure gel. As the gel is surrounded by the pore walls, the network probably reorders to better fit into the given pore space. We hypothesize that this rearrangement additionally affects the bulk relaxation rate for gel in porous media ($1/T_{1,2\ B/GP}$) and call it the *matrix confinement effect* ($X_{1,2\ MC}$). Accordingly, $1/T_{1,2\ B/GP}$ depends on the gel relaxation rate ($1/T_{1,2\ Muc}$) as expressed in Equation 1, and on the matrix confinement effect:

$$\frac{1}{T_{1,2\ B/GP}} = \frac{1}{T_{1,2\ BW}} + G^*_{1,2B} \cdot c_{Muc} + X_{1,2\ MC} \quad (4)$$

The subscript *GP* indicates a porous media filled with gel, and the subscript *MC* refers to the matrix confinement effect. A biohydrogel-containing soil can hold more water than the same soil without biohydrogel at saturation and has, therefore, larger pores than its water-containing equivalent (Chenu, 1993).The type of polymer, its concentration, the soil particle size and its clay content are all factors affecting gel-induced pore expansion (Buchmann and Schaumann, 2017; Chenu, 1993; Kroener et al., 2018; Meyer et al., 2018). Besides, it is not clear how gels swell in the pore system, for example if they undergo expansion into or movement within the pore system. Gel swelling into a cavity is subject to external pressure, which results in an increase of the gel swelling pressure but in a decrease of its equilibrium swelling degree (Kazanskii and Dubrovskii, 1992). To the best of our knowledge, it is not known yet how far external factors specific to field conditions such as confining forces restrict pore expansion coming from soil organic matter and biohydrogel swelling.

In this study, we focused on the quantitative comparison of the water mobility between porous media filled with mucilage and filled with water for several defined particle sizes. For this, the porosity of GB-water and GB-mucilage needed to be similar. For each particle size, the same volumetric amounts of water and mucilage were mixed homogenously with the glass beads. This way, the samples were expected to be under saturated conditions with no swelling effect, and the porosity of GB-water and GB-mucilage was assumed to be similar. Consequently, we hypothesize that an increased surface relaxation in GB-mucilage results from a stronger surface relaxivity: water in gel has a longer rotational correlation time due to interactions with the polymer (Belton et al., 1988; Hills, 1992), so water protons should have

more time to relax at the surface of the particles in comparison to water protons not affected by a polymer network (Brax et al., 2018). The surface relaxivity for gel in porous media ($\rho_{1,2\ GP}$) was hypothesized to depend on the glass beads' surface relaxivity measured in water ($\rho_{1,2\ WP}$) and on an additional parameter ($\rho_{1,2\ \tau c}$) depending on the increase of the rotational correlation time τ_c.

$$\rho_{1,2\ GP} = \rho_{1,2\ WP} + \rho_{1,2\ \tau c} \tag{5}$$

According to our hypotheses, the combination of Equations 2-5 describes R_1 and R_2 of biohydrogel in porous media:

$$\frac{1}{T_{1,2\ GP}} = \frac{1}{T_{1,2\ BW}} + G^*_{1,2\ B} \cdot c_{Muc} + X_{1,2\ MC} + \left(\rho_{1,2\ WP} + \rho_{1,2\ \tau c}\right) \cdot \frac{\beta}{D_{GB}} \tag{6}$$

In order to test these hypotheses, R_1 and R_2 were plotted as a function of the GB size and of the mucilage concentration to consecutively extract and study the polymeric network effect $G^*_{1,2\ B}$, the accelerated surface relaxivity $\rho_{1,2GP}$ and the matrix confinement effect $X_{1,2\ MC}$.

3. Material and methods

3.1. Mucilage preparation

Due to the experimental difficulty to isolate substantial amounts from root mucilage (Zickenrott et al., 2016), chia seed mucilage (*Salvia hispanica L.*) was used: It is easily available in great quantities and shares gel properties such as viscosity relevant to seed, root and microbial exudates in soils (Naveed et al., 2017; Sutherland, 2001). Chia seed mucilage was collected according to the method of Ahmed et al. (2014) and consecutively frozen with liquid nitrogen and freeze-dried. Distilled water was added to the freeze-dried mucilage for it to reswell at concentrations between 0.1 and 1.0 wt%. The samples were left at rest for 48 hours prior to further use for the mucilage to swell completely.

3.2. Glass beads samples preparation

The particle size distribution of the four glass bead particle sizes (soda lime, MHG Strahlanlagen GmbH) was verified under the microscope. For this, glass beads were spread on a glass slide covered with double-sided adhesive tape. Diameters of the glass beads

were measured by means of an ocular micrometer to a get a significant statistical size distribution. The maximal water holding capacity (WHC_{max}) was measured by saturating the samples (three replicates) with the capillary force under free drainage.

(Table 1)

The glass beads were washed successively with 2 M HCl and distilled water and were oven-dried at 105°C for 24 hours. 2 mL of water or chia seed mucilage (0.1-1.0 wt%) were mixed homogeneously with the glass beads in an Eppendorf tube (sample height ca 7 cm, Eppendorf diameter = 1.5 cm), in such a way that the GB-mucilage samples had the same water content as the saturated GB-water samples (Table 1). The samples (three replicates of each) were sealed and stored 48 hours prior to the measurements.

3.3. ^{1}H-NMR relaxometry measurements

Influence of internal field gradients on the relaxation rate. ^{1}H-NMR relaxation data were all collected with a Bruker Minispec MQ at a magnetic field of 0.176 T (proton Larmor frequency of 7.5 MHz). Mitchell et al. (2010) estimated that the largest Larmor frequency at which relaxation from spin diffusion in internal magnetic field is excluded, is 15 MHz for echo times t_E ranging from 2-40 ms. The magnitude of the diffusion relaxation term $1/T_{2D}$ in the NMR response of a sample can be determined by measuring the dependence of R_2 on t_E. To confirm the assumption of Mitchell et al. (2010), a preliminary test was carried out by measuring $R_2$of GB350 saturated with water with a Carr-Purcell-Meiboom-Gill (CPMG) experiment as a function of increasing t_E (0.1-1.2 ms) (Keating and Knight, 2006). Number of scans was 8 and repetition time was set at 10 s to ensure that the samples had returned to thermal equilibrium prior to the start of the pulse sequence. Number of 180° pulses ranged between 50,000 and 10,000 depending on t_E. Variation of t_E did not affect R_2, which remained constant at 0.80±0.05 s^{-1}. In this study, the effect of the diffusion relaxation term on R_2 in this range of t_E is negligible and agrees with the results of Keating and Knight (2006) and Mitchell et al. (2010).

Comparison between 1D and 2D measurements. A further preliminary test was conducted to investigate the potential for systematic errors in the results obtained with two-dimensional (2D) T_1-T_2 correlation experiments (Song et al., 2002) in comparison to the results generated by using a conventional CPMG pulse sequence (Meiboom and Gill, 1958) and inversion recovery (IR) pulse sequence (Void et al., 1967). The measurements were performed on glass beads of two different diameters saturated with 2 mL water. For the 1D and 2D measurements, t_E was 0.3 ms, the repetition time was set at 10 s and gain was 77 such that 80% signal intensity was achieved. Number of scans was 8 for the 1D measurements to ensure a sufficiently high signal-to-noise ratio. Number of 180° pulses ranged between 15,000 (GB90) and 40,000 (GB350) for the CPMG measurement. Inversion time for the inversion recovery (IR) measurement was between 0.3 ms and 15 s with 26 values of T_1. In the 2D correlation measurement, an IR experiment was combined with a simultaneous CPMG pulse sequence (Song et al., 2002). The number of scans was 4 to limit the measurement time to 45 min per sample. CPMG signals were collected for 34 logarithmically spaced values of T_1 with an IR time between 0.3 and 3.67 s for GB90 and 0.6 and 7.3 s for GB350. Number of 180° pulses ranged between 15,000 (GB90) and 20,000 (GB350). The results provided by the 1D and 2D measurements and subsequent data exploitation were the same in the range of the standard deviation for the long R_1 and R_2 values of GB90-water and for the short R_1 and R_2 of GB350-water (see figure in the supporting information). Therefore, no systematic error was produced from the T_1-T_2 correlation measurement or from the 2D-ILT in this study.

2D measurements of the GB-water and GB-mucilage samples. In the 2D correlation experiments carried out for the GB-water and GB-mucilage samples, the IR sequence was composed of 34 logarithmically spaced values of T_1 with an inversion recovery time between 0.6 ms and 7.3 s. Number of 180° pulses ranged between 1200 (GB55) and 9000 (GB2000) with t_E = 0.6 ms. For each experiment, a repetition time of 10 s, 4 scans and a gain of 77 were selected.

Data analysis. All samples were measured in triplicates. CPMG and IR decay curves were analysed with Inverse Laplace Transform (ILT) applied with MATLAB 7.7.0 (R2008b) using the Butler, Reeds and Dawson algorithm (Butler et al., 1981) to generate a relaxation time distribution consisting of 200 exponentially spaced time constants with their associated amplitudes set from 0.1 ms to 10 s (Jaeger et al., 2010). Residual analysis showed that the least deviation occurred for a weight factor of 0.01. The T_1-T_2 correlation maps were obtained with a 2D numerical ILT software provided by Bruker BioSpin and based on the Schlumberger algorithm (Song et al., 2002). The weight factor was set at 1179.77. The samples were assumed to be in the fast diffusion regime so that diffusion between pores could be neglected as each sample exhibited positive signals below the diagonal (Song et al., 2014). The T_1-T_2 maps and the relaxation time distributions from the 1D measurements were all characterized by one main narrow peak. Thus, R_1 and R_2 characterizing each sample were obtained by calculating the average of the three corresponding T_1 and T_2 with the highest signal intensities (Buchmann and Schaumann, 2017; Venkataramanan et al., 2002). R_1 and R_2 were statistically analysed by linear regression and correlation analyses. Variability within the three replicates was presented as the standard deviation. Calculations and figures were made using Microsoft Excel 2007. All raw data are published in Mendeley (http://dx.doi.org/10.17632/52f4t38d9h.1).

3.4. Pulse-field gradient (PFG)-NMR measurements

Description and results of PFG-NMR measurements are in the supporting information.

3.5. Environmental scanning electron microscopy (ESEM)

The preparation of the ESEM samples aimed to reduce the possible changes in the structure of the polymer network. For this, GB55 and GB350 mixed with 0.1 wt% and 1.0 wt% mucilage were immersed into liquid nitrogen prior to freeze-drying to avoid a glass transition of the polymer and to preserve the original structure of the mucilage network from the wet in the dry state.. ESEM images were taken with an FEI Quanta 250 ESEM (FEI Company

Hillsboro, United States) under low vacuum with chamber pressures between 60 and 80 Pa. A large field detector was used with an acceleration voltage between 12.5 and 15 kV.

3.6. X-ray computed microtomography

The inner spatial structure of GB350 mixed respectively with water, 0.1wt% and 1.0wt% mucilage was analyzed by µCT using an industrial scanner (X-Tek XT H 225, Nikon Metrology GmbH). For preserving a good contrast, a relatively low voltage of 90 kV and a current of 205 µA were applied and no filter was used. An entire µCT scan comprised 2000 projections at an exposure time of 708 ms and took 25 min. The flat panel X-ray detector (PerkinElmer 1620) with 1750 by 2000 pixels captured the images at a spatial resolution of 9 µm and 8 bit grayscale resolution. The reconstruction of three-dimensional images via filtered back projection was done using the CT Pro 3-D software package (version 3.1, Nikon Metrology). Only the middle part of the vials was captured due to the limited size of the field of view. This corresponded roughly to one third of the total sample volume of about 8 cm^3, and an inner cylindrical region of interest (ROI) of 1.5 to 2 cm^3 was analyzed out of it to exclude wall effects in the images.

3.7. Image processing and analysis

Image analysis was conducted to analyze the three-phase system composed of glass beads, water/mucilage and air. From the image analysis, the size distributions of particles, pores, and air bubbles within the pore space were calculated. The image processing workflow was done using the Image-J software package (Schindelin et al., 2012). Noise was first removed with a nonlocal means filter (Tristán-Vega et al., 2012). Next, the thresholds segmenting air, water/mucilage and particles were manually set based on visual comparison of the filtered grayscale image and the segmented image. This manual segmentation gave more consistent results than our usually applied combination of different histogram evaluation methods (Schlüter et al., 2014). Markov random field segmentation was then used for image segmentation (Kulkarni et al., 2012). Finally, Euclidean distance mapping as included in the

322 "Local Thickness Plugin" in ImageJ (Dougherty and Kunzelmann, 2007) was applied to the
323 segmented binary CT images to obtain pore size distributions.

324 4. Results and discussion

325 *4.1. Structure of the mucilage network in porous media*

326 Figure 2 shows the ESEM pictures of N_2 (l) freeze-dried GB55 mixed with 0.1 wt% (Fig. 2a)
327 and with 1.0 wt% mucilage (Fig. 2b).

328 (**Figure 2)**

329 Lone discrete polymer strands depicted by the white lines were sparsely distributed on the
330 surface of the particles in GB55 mixed with 0.1 wt% mucilage. They appeared to be more
331 abundant with branched structures in GB55 mixed with 1.0 wt% mucilage. Whereas no
332 polymer network was visible in the pore space in GB55 mixed with 0.1 wt% mucilage,
333 polymer strands linked the particles in GB55 mixed with 1.0 wt% mucilage and a porous
334 polymer network was only observed in the biggest pore (top left). Instead of covering the
335 particle surface as in GB55 mixed with 0.1 wt% mucilage, the polymer agglomerated in the
336 pore space in GB350 mixed with 0.1 wt% mucilage and formed a clear-cut network
337 seemingly brittle. It is not clear from the picture whether it was attached to other beads or
338 not. In GB350 mixed with 1.0 wt% mucilage, the polymer built a dense organized porous
339 network in the pore space, whose extremities appeared to take anchor at the surface of the
340 particles.

341 Imaging dry hydrogel networks with the ESEM is subject to artefacts: Ice crystal formation
342 during the freeze-drying step and aggregation or collapse of the polymer network under
343 vacuum cannot be discarded (Hills et al., 2000; Mao et al., 2001). Although shock-freezing
344 directly followed by freeze-drying reduces the formation of ice crystals in comparison to slow
345 freezing (Belton et al., 1988; Hills et al., 2000), information from the images must be
346 considered cautiously. GB55 and GB350 had similar water content (Table 1), but GB55 had
347 more and smaller pores than GB350. Nevertheless, mucilage was distributed

348 homogeneously within both systems. As mucilage is a shear-thinning gel at these
349 concentrations (Capitani et al., 2015), i.e. its viscosity decreases under shear strain, the
350 polymer chains are flexible and deformable and have the capacity to change their
351 conformation to adapt to the pore space. Figures 2a-d suggested that the organization of the
352 polymer network was pore size dependent: it extended in discrete strands at low
353 concentrations and built bridges between the particles at higher concentrations for GB55.
354 The higher number of pores of GB55 implies a lower amount of polymer per pore, which
355 probably prevents polymer agglomeration and explains the absence of porous network in
356 most pores. Another reason could be that the optimal size formed by the polymeric network
357 is bigger than the available space between GB55 particles. In fact, already at low mucilage
358 concentration for GB350, the polymer takes advantage of the pore space to expand and form
359 an organized structure. The polymeric meshes gain in structure and density with increasing
360 mucilage concentration. Finally, in GB55 and GB350 mixed with the highest mucilage
361 concentration, the polymer strands seemed to grip the surface of the particles and thus may
362 have strained the network across the pore and increased its rigidity.

363 The ESEM pictures of the glass beads suggested qualitatively that the polymer network
364 depends on the particle size and varies with the polymer concentration. If so, these variations
365 of the polymer network should affect the water mobility expressed by the relaxation rate.

366 *4.2. Water mobility in porous systems filled with water and mucilage*

367 According to Equations 2 and 3, the relaxation rate is expressed as a function of the
368 reciprocal particle diameter. R_1 (Fig. 3a) and R_2 (Fig. 3b) of GB-water and GB-mucilage from
369 the 2D experiments were therefore plotted as a function of the reciprocal glass beads
370 diameter. In Figure 3a, R_1 increased with the mucilage concentration for the two larger glass
371 beads. R_1 of GB150 decreased slightly for concentrations until 0.5 wt% and jumped to a
372 higher relaxation rate for the highest concentration. R_1 decreased with increasing mucilage
373 concentration for GB55. Corresponding R_2 behaved differently than R_1: increasing mucilage

concentration lead to higher R_2 for all glass beads, though the strength with which R_2 increased varied with the particles' diameter.

(Figure 3)

The two gel effects identified by Brax et al. (2018) predict higher relaxation rates when mucilage replaced water in a porous system due to an increase of the bulk relaxation and of the surface relaxivity. The diverging trends between R_1 and R_2 for the smallest glass beads suggest the existence of distinct processes affecting R_1 and R_2 differently. A solid-like relaxation behaviour characterized by slow R_1 coupled with fast R_2 for the smallest beads at high mucilage concentration is unlikely: For the same volume and concentration of mucilage mixed with the glass beads, there is less polymeric material in the small pores of GB55 than in the big pores of GB350. Another explanation for the unexpected decrease of R_1 with increasing mucilage concentration might be a distortion of the pore size distribution in GB55. Swelling of biohydrogel or organic matter in soil was shown to result in an expansion of the small pores and thus to a shift of the relaxation rate (Jaeger et al., 2010b; Meyer et al., 2018; Todoruk et al., 2003). However, the effect of the increase of the polymer concentration on the pore size distribution by constant water content is not clear and has not been yet investigated to the best of our knowledge. By constant water content, mucilage at high concentration might push the beads aside to create bigger pores, in which the polymer network can expand. This distortion of the pores would affect GB55 stronger than the bigger glass beads. One reason could be that the pores in GB55 being much smaller than those of the bigger beads, the urge of mucilage to expand is stronger in the smaller pores than in the bigger pores. Another reason could be that the smaller volume and lighter weight of GB55 make it easier for mucilage to push the particles asides. This distortion of the pores would have occurred although our aim was to have the same pore size distribution for the GB-water and GB-mucilage samples at all mucilage concentrations.

In order to assess a hypothetical change of the pore size, µCT images were scanned for GB55 and GB350 mixed with water, mucilage 0.25 wt%, and mucilage 1.0 wt%. The µCT

parameters did not permit to distinguish the particles from water for GB55 due to the limits of resolution (supporting information).

(Figure 4)

Figure 4a characterized the volumetric pore size distribution (PSD) of water- and mucilage-filled pores in GB350, and Figure 4b depicted the volumetric size distribution of air bubbles in GB350. The data presented refer to 2000 mm^3 samples. Considering the variations within the samples, the PSD of water- and mucilage-filled pores in GB350 were similar. Although the diameter of the air bubbles decreased and the number of the air bubbles increased from GB350 mixed with water to GB350 mixed with mucilage 1.0 wt%, the air bubbles had no influence on the PSD of GB350. One effect of the air bubbles could be an additional paramagnetic relaxation from dissolved oxygen in the samples with more air bubbles. However, additional paramagnetic relaxation leads to faster R_1 (Mirhej, 1965), while the effects observed were a reduction of R_1 and an increase of R_2. Another effect of the air bubbles can be the increase of R_2 because of magnetic susceptibility differences arising from the additional interfaces (Alexander et al., 1996). Thus, the increase of R_2 despite the decrease of R_1 for GB55 at increasing mucilage concentration could come from the increased sensitivity of R_2 to the mucilage concentration and from the magnetic susceptibility related to the air bubbles.

Due to its viscosity, hydrated mucilage cannot be mixed with the glass beads by capillary forces as it can be done for water. Kroener et al. (2014) applied an alternative method consisting of mixing the swollen gel with the glass beads and drying the mixture in the oven. Once dried, the samples were watered by capillary rise. This procedure does not allow the fulfillment of several conditions, which are necessary to study the samples by means of our conceptual model: all samples must have the same amount of water, the mucilage concentration should not vary depending on its position in the sample, and the mucilage need to be homogeneously distributed in the pores and at their surface. The addition of a controlled quantity of water to the glass beads and thorough homogenization of the samples

appear therefore as the method of choice. Additional application of a suction to get rid of the air bubbles and to drain the samples to a pendular bridge state could be considered in a next experiment, given this method does not modify the spatial distribution of mucilage in the samples.

4.3. Influence of the mucilage concentration on the R_1 and the R_2 for all glass beads

The ESEM images (Fig. 2) suggest the organization of the polymer in the pore space depends on the particle size. Derivation of the polymeric network effect $G^*_{1,2\,B}$ from R_1 and R_2 for each particle size would enable verification of this aspect and its effect on the relaxation rate. For this, R_1 and R_2 were plotted as a function of the mucilage concentration for each particle size. The slope corresponds to the polymeric network effect $G^*_{1,2\,B}$ according to Equation 6. The linear relationships between $R_{1,2}$ and the mucilage concentration were analysed for each particle size by means of the statistical parameters listed in Table 2.

(Table 2)

R_1 increased with increasing mucilage concentration for GB2000, GB350 and GB150, and decreased with increasing mucilage concentration for GB55. For R_1, R^2 and the significance of the proportional relationship (Pearson R, p) decreased from GB2000 to GB150. R_2 increased with increasing mucilage concentration for all particles. For R_2, the significance of the proportional relationship decreased for GB55.

The decrease of R_1 for GB55-mucilage despite the increase of the mucilage concentration may come from the formation of bigger pores, either due to a disturbance because of the multiplication of the air bubbles or to a distortion of the pores originated by the mucilage itself.

The polymeric network effects on R_1 ($G^*_{1\,B}$) (Fig. 5a) and on the R_2 ($G^*_{2\,B}$) (Fig. 5b) were plotted against the particle diameter. Values of $G^*_{1,2\,B}$ in pure mucilage were from Brax et al. (2018). $G^*_{2\,B}$ was higher than $G^*_{1\,B}$ for pure mucilage. $G^*_{1\,B}$ for glass beads comprised

between 150 and 2000 µm was similar to $G^*_{1\,B}$ for pure mucilage, but $G^*_{1\,B}$ for GB55 was negative. The particle size affected $G^*_{1\,B}$ differently than $G^*_{2\,B}$: $G^*_{2\,B}$ for GB2000 was similar to $G^*_{2\,B}$ for pure mucilage and then increased with decreasing particle size until GB150. $G^*_{2\,B}$ dropped for GB55.

(Figure 5)

Combination with the previous results suggests that $G^*_{1,2\,B}$ does not only reflect the polymeric network effect but results from a distortion of the pores. The negative value of $G^*_{1\,B}$ for GB55 shows that this distortion affects the R_1 more than the polymeric network effect does. The behavior of $G^*_{2\,B}$ indicates that the R_2 is more sensitive to the polymeric network than the R_1. Indeed, transverse relaxation depends on direct interactions between the spins of the water protons and the ones of the polymer protons without the energy transfer required for longitudinal relaxation (Belton et al., 1988).

The increase of $G^*_{2\,B}$ with decreasing pore size probably corresponds to the rearrangement of the polymer in a stiffer network, as illustrated in Figure 6. In Figure 6b, the inter-particle pore is several times larger than the pores formed by the pure mucilage (Fig. 6a): the network organization of the free polymer and of the polymer trapped in big pores changes little. Figure 6b could schematize GB2000-mucilage. In Figure 6c, decreasing inter-particle pore affects more and more the organization of the polymer network: the polymer rearranges to form smaller pores. Rearrangement of the polymer network leads to the increase of the R_2. The drop of $G^*_{2\,B}$ for GB55 is linked with the distortion of the pores, but also suggests that the opposite effect took place for very small particles: the low concentration of polymer per pores combined with the pore smallness prevents the organization of the polymer in a network (Fig. 6d).

(Figure 6)

4.4. Influence of the mucilage concentration on the surface relaxivity and the matrix confinement effect

In order to investigate how the mucilage concentration affects the surface relaxivity and the bulk relaxation, R_1 and R_2 were expressed as a function of the inverse of the GB diameter (Equation 6). The statistical values (supporting information) indicated the linear relationship between R_1, R_2 and the reciprocal GB diameter were significant for all mucilage concentrations. According to Equations 2,3 and 6, the slope corresponds to $\beta \cdot \rho_{1,2\,WP}$ for GB-water and to $\beta \cdot (\rho_{1,2\,WP} + \rho_{1,2\,\tau c})$ for GB-mucilage: The slope captures the influence of the mucilage concentration on the surface relaxivity coupled with the pore size proportional factor β and was plotted against the mucilage concentration in Figure 7.

(Figure 7)

The values of $\beta \cdot \rho$ for R_1 lowered with increasing mucilage concentration, while the values of $\beta \cdot \rho$ for R_2 stayed similar over the concentration range of mucilage.

Previous observations (Fig. 2-5) suggested an increase of the pore size for the smallest particles at higher mucilage concentrations. This would imply a drop of the pore size proportional factor β for the smallest particles (Equation 3). The overall $\beta \cdot \rho_{1,2}$ would be then subjected to two opposite trends with higher mucilage concentrations: increase of $\rho_{1,2}$ and decrease of β. In Figure 7, the decrease of β seems to influence the longitudinal $\beta \cdot \rho_1$ stronger than the transverse $\beta \cdot \rho_2$, for which both trends seem to be balanced. These results suggest that ρ_2 is more sensitive than ρ_1 to the gel effect. The results also propose that the acceleration of the surface relaxation identified by Brax et al. (2018) might not be significant to detect and describe mucilage in porous medium: isolation of ρ from β was not possible and the variation of ρ was shielded by the decrease of β.

According to Equation 6, the y-intercepts of the R_1 and of the R_2 as a function of the reciprocal GB diameter correspond to the bulk relaxation rates $1/T_{1,2\,B/WP}$ for GB-water and $1/T_{1,2\,B/GP}$ for GB-mucilage. The bulk relaxation rates are expressed by $1/T_{1,2\,BW}$ for GB-water and by $1/T_{1,2\,B/WP} + G^*_{1,2\,B} \cdot c_{muc} + X_{1,2\,MC}$ for GB-mucilage (Equations 2, 3 and 6). They

were plotted against the mucilage concentration in Figure 8. The R_1 and the R_2 of pure mucilage were described by $1/T_{1,2\,BW} + G^*_{1,2\,B} \cdot c_{muc}$ (Equation 1) and were plotted on Figure 8 to highlight $G^*_{1,2\,B}$ and $X_{1,2\,MC}$ in porous media.

(Figure 8)

The slopes for GB-mucilage, ($G^*_{1\,B}$ = 0.23 +/- 0.04 s^{-1}·wt%$^{-1}$ and $G^*_{2\,B}$ =0.60 +/- 0.06 s^{-1}·wt%$^{-1}$) were higher than the slopes for pure mucilage ($G^*_{1\,B}$ =0.10+/- 0.00 s^{-1}·wt%$^{-1}$ and $G^*_{2\,B}$ =0.41 +/- 0.00 s^{-1}·wt%$^{-1}$). The same trend was observed for the y-intercepts of GB-mucilage ($1/T_{1\,BW} + X_{1\,MC}$= 0.42 +/- 0.03 s^{-1} and $1/T_{2\,BW} + X_{2\,MC}$= 0.47 +/- 0.04 s^{-1}) and pure mucilage ($1/T_{1\,BW}$= 0.38 +/-0.00 s^{-1} and $1/T_{2\,BW}$= 0.41 +/- 0.00 s^{-1}), which implies that the matrix confinement effect $X_{1,2\,MC}$ is larger than zero.

These results suggest that the polymeric network in porous GB medium affects proton relaxation stronger than the polymeric network in free mucilage. This observation is explained by the spider-web effect, translated by an increase of rigidity of the polymer strands in the porous medium: while polymer strands do not have volume restriction in the free mucilage, the walls of the particles restrict the elongation of the polymer strands in a porous medium. These walls also serve as a frame for the polymer porous network, thus conferring rigidity to the polymer strands. The spider-web effect is translated by an increase of $G^*_{1,2}$ with the mucilage concentration and by $X_{1,2\,MC}$ larger than zero.

Finally, our conceptual model describing the gel effect on the NMR parameters offers a quantitative analysis of the shift of the relaxation rate due to the presence of mucilage in porous media. The interpretation of results showed a pore-size specific organization of the polymeric network, which suggested that the gel effect on further soil properties also depends on the particle size. A similar concept was presented by Kroener et al. (2018), who found that the effect of chia seed mucilage on saturated hydraulic conductivity was particle size specific.

In a next step, the method should be applied to root exudates and mucilages and to soil samples with increasing complexity regarding pore size distribution and organic matter content. A further challenge is also to develop the detection and characterization of mucilage when present as a biohydrogel phase in the soil medium. The change of mucilage properties after drying and rewetting also needs to be understood, given experiments showed that the rewetting of biohydrogel phases in soil leads to a change of the macroscopic properties (Buchmann et al., 2015a).

5. Conclusion

In conclusion, the combination of ^{1}H NMR and ESEM images showed that the organization of the mucilage network depends on the particle size. The *polymeric network effect* was stronger in the porous medium of particles between 150 and 350 µm and dropped for very fine and very coarse particles. Accordingly, it would be interesting to measure the hydraulic conductivity at several mucilage concentrations and investigate a correlation between the water mobility measured with ^{1}H NMR and the hydraulic conductivity.

Slow R_1 and fast R_2 suggested a distortion of the pores for the smaller glass beads at high mucilage concentrations, which needs to be verified by additional experiments. This alteration from our defined samples helps to highlight and to discriminate between several gel effects and their relative influence on longitudinal and transverse relaxation. *Accelerated surface relaxation* is not validated as a significant gel effect, as both R_1 and R_2 seem to be more affected by the pore distortion than by the increase of the surface relaxivity ρ related to the gel effect. On the contrary, *accelerated bulk relaxation* is a significant gel effect: it is composed of the *polymeric network effect*, which carries information about the concentration of mucilage in the pore and organization of the polymer network in the pore. The *accelerated bulk relaxation* also brings to evidence a *spider-web effect*, which attests the additional rigidity of the polymer network due to its strands spanned in the pore space, as opposed to unattached and loose strands in the free gel. Finally, the transverse bulk relaxation was more affected by these gel effects than the longitudinal relaxation.

(Table 3)

6. References

Ahmed, M.A., Kroener, E., Benard, P., Zarebanadkouki, M., Kaestner, A., Carminati, A., 2016. Drying of mucilage causes water repellency in the rhizosphere of maize: measurements and modelling. Plant Soil 407, 161–171. https://doi.org/10.1007/s11104-015-2749-1

Ahmed, M.A., Kroener, E., Holz, M., Zarebanadkouki, M., Carminati, A., 2014. Mucilage exudation facilitates root water uptake in dry soils. Funct. Plant Biol. 41, 1129. https://doi.org/10.1071/FP13330

Albalasmeh, A.A., Ghezzehei, T.A., 2014. Interplay between soil drying and root exudation in rhizosheath development. Plant Soil 374, 739–751. https://doi.org/10.1007/s11104-013-1910-y

Alexander, A.L., McCreery, T.T., Barrette, T.R., Gmitro, A.F., Unger, E.C., 1996. Microbubbles as novel pressure-sensitive MR contrast agents. Magn. Reson. Med. 35, 801–806. https://doi.org/10.1002/mrm.1910350603

Bayer, J.V., Jaeger, F., Schaumann, G.E., 2010. Proton nuclear magnetic resonance (NMR) relaxometry in soil science applications. Open Magn. Reson. J. 3, 15–26.

Belton, P.S., Hills, B.P., Raimbaud, E.R., 1988. The effects of morphology and exchange on proton NMR relaxation in agarose gels. Mol. Phys. 63, 825–842.

Brax, M., Buchmann, C., Schaumann, G.E., 2018. Effect of mucilage on water properties in the rhizosphere monitored by 1H-NMR relaxometry. Microporous Mesoporous Mater., Proceedings of the 13th International Bologna Conference on Magnetic Resonance in Porous Media (MRPM13) 269, 47–50. https://doi.org/10.1016/j.micromeso.2017.07.044

Brax, M., Buchmann, C., Schaumann, G.E., 2017. Biohydrogel induced soil–water interactions: how to untangle the gel effect? A review. J. Plant Nutr. Soil Sci. 180, 121–141. https://doi.org/10.1002/jpln.201600453

Brownstein, K.R., Tarr, C.E., 1979. Importance of classical diffusion in NMR studies of water in biological cells. Phys. Rev. A 19, 2446.

Buchmann, C., Bentz, J., Schaumann, G.E., 2015a. Intrinsic and model polymer hydrogel-induced soil structural stability of a silty sand soil as affected by soil moisture dynamics. Soil Tillage Res. 154, 22–33. https://doi.org/10.1016/j.still.2015.06.014

Buchmann, C., Meyer, M., Schaumann, G.E., 2015b. Characterization of wet aggregate stability of soils by H-NMR relaxometry. Magn. Reson. Chem. 53, 694–703. https://doi.org/10.1002/mrc.4147

Buchmann, C., Schaumann, G.E., 2017. Effect of water entrapment by a hydrogel on the microstructural stability of artificial soils with various clay content. Plant Soil 414, 181–198. https://doi.org/10.1007/s11104-016-3110-z

Butler, J., Reeds, J., Dawson, S., 1981. Estimating Solutions of First Kind Integral Equations with Nonnegative Constraints and Optimal Smoothing. SIAM J. Numer. Anal. 18, 381–397. https://doi.org/10.1137/0718025

Capitani, M.I., Corzo-Rios, L.J., Chel-Guerrero, L.A., Betancur-Ancona, D.A., Nolasco, S.M., Tomás, M.C., 2015. Rheological properties of aqueous dispersions of chia (Salvia hispanica L.) mucilage. J. Food Eng. 149, 70–77. https://doi.org/10.1016/j.jfoodeng.2014.09.043

Carminati, A., 2012. A Model of Root Water Uptake Coupled with Rhizosphere Dynamics. Vadose Zone J. 11, 0. https://doi.org/10.2136/vzj2011.0106

Carminati, A., Schneider, C.L., Moradi, A.B., Zarebanadkouki, M., Vetterlein, D., Vogel, H.-J., Hildebrandt, A., Weller, U., Schüler, L., Oswald, S.E., 2011. How the Rhizosphere May Favor Water Availability to Roots. Vadose Zone J. 10, 988–998. https://doi.org/10.2136/vzj2010.0113

608 Carminati, A., Vetterlein, D., 2013. Plasticity of rhizosphere hydraulic properties as a key for
609 efficient utilization of scarce resources. Ann. Bot. 112, 277–290.
610 https://doi.org/10.1093/aob/mcs262
611 Chenu, C., 1993a. Clay-or sand-polysaccharide associations as models for the interface
612 between micro-organisms and soil: water related properties and microstructure.
613 Geoderma 56, 143–156.
614 Chui, M.M., Phillips, R.J., McCarthy, M.J., 1995. Measurement of the porous microstructure
615 of hydrogels by nuclear magnetic resonance. J. Colloid Interface Sci. 174, 336–344.
616 Codd, S.L., Vogt, S.J., Hornemann, J.A., Phillips, A.J., Maneval, J.E., Romanenko, K.R.,
617 Hansen, L., Cunningham, A.B., Seymour, J.D., 2011. NMR relaxation measurements
618 of biofouling in model and geological porous media. Org. Geochem., Applications and
619 developments of magnetic resonance techniques in Geosciences 42, 965–971.
620 https://doi.org/10.1016/j.orggeochem.2011.03.014
621 Davit, Y., Iltis, G., Debenest, G., Veran-Tissoires, S., Wildenschild, D., Gerino, M., Quintard,
622 M., 2011. Imaging biofilm in porous media using X-ray computed microtomography. J.
623 Microsc. 242, 15–25. https://doi.org/10.1111/j.1365-2818.2010.03432.x
624 Dougherty, R., Kunzelmann, K.-H., 2007. Computing Local Thickness of 3D Structures with
625 ImageJ. Microsc. Microanal. 13, 1678–1679.
626 https://doi.org/10.1017/S1431927607074430
627 Dunn, K.-J., Bergman, D.J., LaTorraca, G.A., 2002. Nuclear magnetic resonance:
628 petrophysical and logging applications. Pergamon, New York.
629 Godefroy, S., Korb, J.-P., Fleury, M., Bryant, R.G., 2001. Surface nuclear magnetic
630 relaxation and dynamics of water and oil in macroporous media. Phys. Rev. E 64,
631 021605. https://doi.org/10.1103/PhysRevE.64.021605
632 Gregory, P. j., 2006. Roots, rhizosphere and soil: the route to a better understanding of soil
633 science? Eur. J. Soil Sci. 57, 2–12. https://doi.org/10.1111/j.1365-2389.2005.00778.x
634 Helliwell, J.R., Sturrock, C.J., Grayling, K.M., Tracy, S.R., Flavel, R.J., Young, I.M., Whalley,
635 W.R., Mooney, S.J., 2013. Applications of X-ray computed tomography for examining
636 biophysical interactions and structural development in soil systems: a review. Eur. J.
637 Soil Sci. 64, 279–297. https://doi.org/10.1111/ejss.12028
638 Hills, B.P., 1992. The proton exchange cross-relaxation model of water relaxation in
639 biopolymer systems. Mol. Phys. 76, 489–508.
640 Hills, B.P., Godward, J., Debatty, M., Barras, L., Saturio, C.P., Ouwerx, C., 2000. NMR
641 studies of calcium induced alginate gelation. Part II. The internal bead structure.
642 Magn. Reson. Chem. 38, 719–728.
643 Jaeger, F., Grohmann, E., Schaumann, G.E., 2006. 1H NMR Relaxometry in natural humous
644 soil samples: Insights in microbial effects on relaxation time distributions. Plant Soil
645 280, 209–222. https://doi.org/10.1007/s11104-005-3035-4
646 Jaeger, F., Shchegolikhina, A., Van As, H., Schaumann, G.E., 2010. Proton NMR
647 relaxometry as a useful tool to evaluate swelling processes in peat soils. Open Magn.
648 Reson. J. 3, 27–45.
649 Kazanskii, K.S., Dubrovskii, S.A., 1992. Chemistry and physics of “agricultural” hydrogels, in:
650 Polyelectrolytes Hydrogels Chromatographic Materials. Springer Berlin Heidelberg,
651 pp. 97–133.
652 Keating, K., Knight, R., 2006. A laboratory study to determine the effect of iron oxides on
653 proton NMR measurements. GEOPHYSICS 72, E27–E32.
654 https://doi.org/10.1190/1.2399445
655 Kirkland, C.M., Hiebert, R., Phillips, A., Grunewald, E., Walsh, D.O., Seymour, J.D., Codd,
656 S.L., 2015. Biofilm Detection in a Model Well-Bore Environment Using Low-Field
657 NMR. Groundw. Monit. Remediat. 35, 36–44. https://doi.org/10.1111/gwmr.12117
658 Kleinberg, R.L., 1996. Utility of NMR T2 distributions, connection with capillary pressure, clay
659 effect, and determination of the surface relaxivity parameter rho 2. Magn. Reson.
660 Imaging 14, 761–767.
661 Kleinberg, R.L., Kenyon, W.E., Mitra, P.P., 1994. Mechanism of NMR relaxation of fluids in
662 rock. J. Magn. Reson. A 108, 206–214.

Kroener, E., Holz, M., Zarebanadkouki, M., Ahmed, M., Carminati, A., 2018. Effects of mucilage on rhizosphere hydraulic functions depend on soil particle size. Vadose Zone J. 17.

Kroener, E., Zarebanadkouki, M., Kaestner, A., Carminati, A., 2014. Nonequilibrium water dynamics in the rhizosphere: How mucilage affects water flow in soils. Water Resour. Res. 50, 6479–6495. https://doi.org/10.1002/2013WR014756

Kulkarni, R., Tuller, M., Fink, W., Wildenschild, D., 2012. Three-dimensional multiphase segmentation of X-ray CT data of porous materials using a Bayesian Markov random field framework. Vadose Zone J. 11. https://doi.org/10.2136/vzj2011.0082

Li, B., Ding, D., Wang, Y., Sun, P., Ma, J., He, B., 1999. NMR characterization of absorbed water in equilibrium swollen hydrogel P(AM-NaA). J. Appl. Polym. Sci. 72, 1203–1207. https://doi.org/10.1002/(SICI)1097-4628(19990531)72:9<1203::AID-APP9>3.0.CO;2-R

Lüsse, S., Arnold, K., 1998. Water Binding of Polysaccharides: NMR and ESR Studies. Macromolecules 31, 6891–6897. https://doi.org/10.1021/ma971869d

Mao, R., Tang, J., Swanson, B.G., 2001. Water holding capacity and microstructure of gellan gels. Carbohydr. Polym. 46, 365–371. https://doi.org/10.1016/S0144-8617(00)00337-4

Meiboom, S., Gill, D., 1958. Modified Spin-Echo Method for Measuring Nuclear Relaxation Times. Rev. Sci. Instrum. 29, 688–691. https://doi.org/10.1063/1.1716296

Meyer, M., Buchmann, C., Schaumann, G.E., 2018. Determination of quantitative pore-size distribution of soils with 1H NMR relaxometry. Eur. J. Soil Sci. 69, 393–406. https://doi.org/10.1111/ejss.12548

Mirhej, M.E., 1965. Proton Spin relaxation by paramagnetic molecular oxygen. Can. J. Chem. 43, 1130–1138.

Mitchell, J., Chandrasekera, T.C., Johns, M.L., Gladden, L.F., Fordham, E.J., 2010. Nuclear magnetic resonance relaxation and diffusion in the presence of internal gradients: the effect of magnetic field strength. Phys. Rev. E Stat. Nonlin. Soft Matter Phys. 81, 026101. https://doi.org/10.1103/PhysRevE.81.026101

Naveed, M., Brown, L.K., Raffan, A.C., George, T.S., Bengough, A.G., Roose, T., Sinclair, I., Koebernick, N., Cooper, L., Hackett, C.A., Hallett, P.D., 2017. Plant exudates may stabilize or weaken soil depending on species, origin and time. Eur. J. Soil Sci. 68, 806–816. https://doi.org/10.1111/ejss.12487.

Sanderlin, A.B., Vogt, S.J., Grunewald, E., Bergin, B.A., Codd, S.L., 2013. Biofilm detection in natural unconsolidated porous media using a low-field magnetic resonance system. Environ. Sci. Technol. 47, 987–992. https://doi.org/10.1021/es3040686

Schindelin, J., Arganda-Carreras, I., Frise, E., Kaynig, V., Longair, M., Pietzsch, T., Preibisch, S., Rueden, C., Saalfeld, S., Schmid, B., Tinevez, J.-Y., White, D.J., Hartenstein, V., Eliceiri, K., Tomancak, P., Cardona, A., 2012. Fiji: an open-source platform for biological-image analysis. Nat. Methods 9, 676–682. https://doi.org/10.1038/nmeth.2019

Schlüter, S., Sheppard, A., Brown, K., Wildenschild, D., 2014. Image processing of multiphase images obtained via X-ray microtomography: A review. Water Resour. Res. 50, 3615–3639. https://doi.org/10.1002/2014WR015256

Shapiro, Y.E., 2011. Structure and dynamics of hydrogels and organogels: An NMR spectroscopy approach. Prog. Polym. Sci. 36, 1184–1253. https://doi.org/10.1016/j.progpolymsci.2011.04.002

Song, Y.-Q., Carneiro, G., Schwartz, L.M., Johnson, D.L., 2014. Experimental identification of diffusive coupling using 2D NMR. Phys. Rev. Lett. 113, 235503. https://doi.org/10.1103/PhysRevLett.113.235503

Song, Y.-Q., Venkataramanan, L., Hürlimann, M.D., Flaum, M., Frulla, P., Straley, C., 2002. T1–T2 Correlation Spectra Obtained Using a Fast Two-Dimensional Laplace Inversion. J. Magn. Reson. 154, 261–268. https://doi.org/10.1006/jmre.2001.2474

Sutherland, I., 2001. Biofilm exopolysaccharides: a strong and sticky framework. Microbiol. Read. Engl. 147, 3–9. https://doi.org/10.1099/00221287-147-1-3

Todoruk, T.R., Langford, C.H., Kantzas, A., 2003. Pore-scale redistribution of water during wetting of air-dried soils as studied by low-field NMR relaxometry. Environ. Sci. Technol. 37, 2707–2713.

Tristán-Vega, A., García-Pérez, V., Aja-Fernández, S., Westin, C.-F., 2012. Efficient and robust nonlocal means denoising of MR data based on salient features matching. Comput. Methods Programs Biomed. 105, 131–144. https://doi.org/10.1016/j.cmpb.2011.07.014

Venkataramanan, L., Song, Y.-Q., Hurlimann, M.D., 2002. Solving Fredholm integrals of the first kind with tensor product structure in 2 and 2.5 dimensions. IEEE Trans. Signal Process. 50, 1017–1026. https://doi.org/10.1109/78.995059

Void, R.L., Waugh, J.S., Klein, M.P., Phelps, D.E., 1967. Measurement of spin relaxation in complex systems.

Zarebanadkouki, M., Kim, Y.X., Moradi, A.B., Vogel, H.-J., Kaestner, A., Carminati, A., 2012. Quantification and Modeling of Local Root Water Uptake Using Neutron Radiography and Deuterated Water. Vadose Zone J. 11, vzj2011.0196. https://doi.org/10.2136/vzj2011.0196

Zickenrott, I.-M., Woche, S.K., Bachmann, J., Ahmed, M.A., Vetterlein, D., 2016. An efficient method for the collection of root mucilage from different plant species—A case study on the effect of mucilage on soil water repellency. J. Plant Nutr. Soil Sci. 179, 294–302. https://doi.org/10.1002/jpln.201500511

Figure captions

Figure 1: Visualisation of bulk relaxation and surface relaxation in a pore filled with water (a) and the same pore filled with a polymeric network (b).

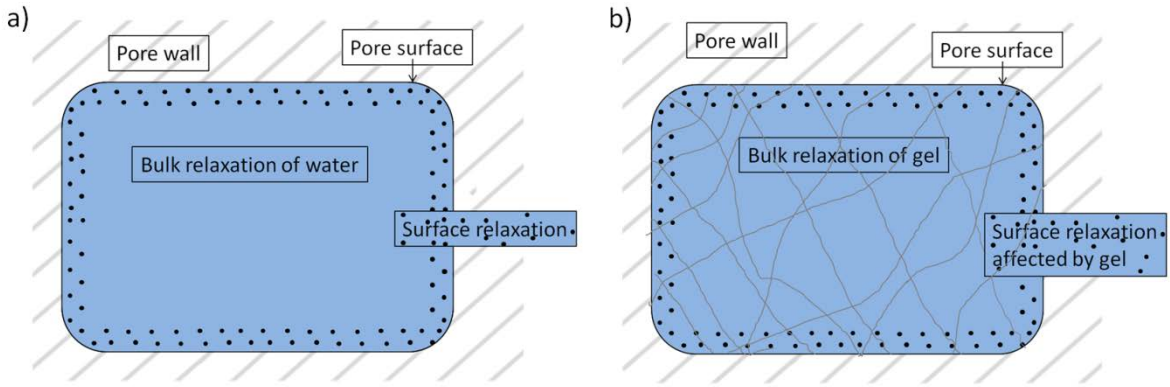

Figure 2: ESEM pictures of GB55 mixed with 0.1% (a) and 1.0% (b) mucilage, and of GB350 mixed with 0.1% (c) and 1.0% (d) mucilage.

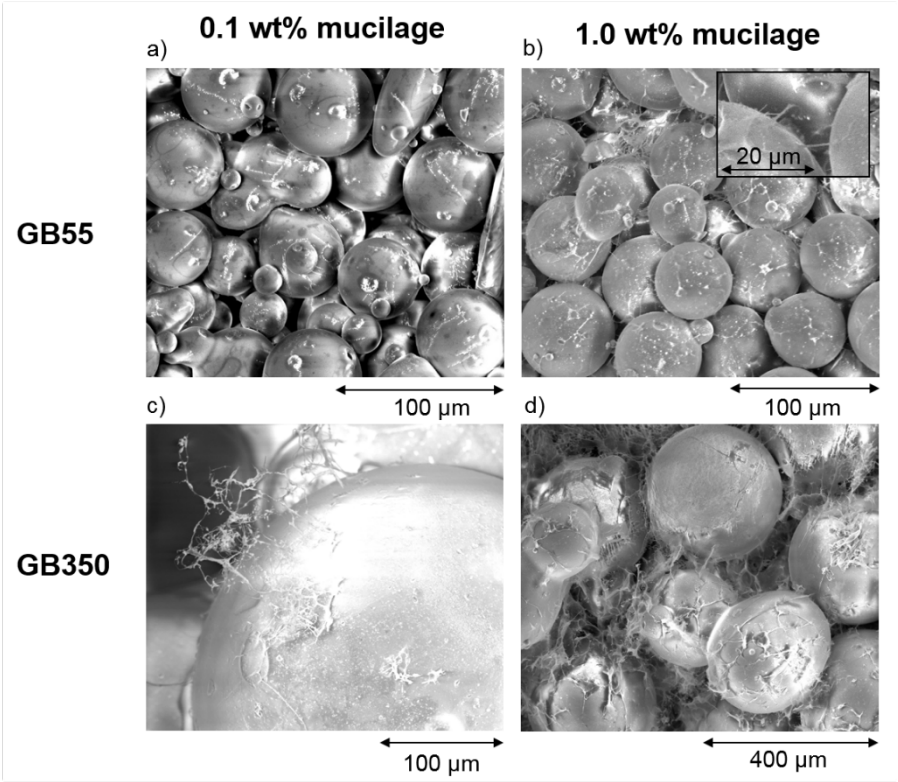

Figure 3: Variation of the longitudinal (a) and transversal (b) relaxation rates as a function of the reciprocal GB diameter for water and mucilage at several concentrations.

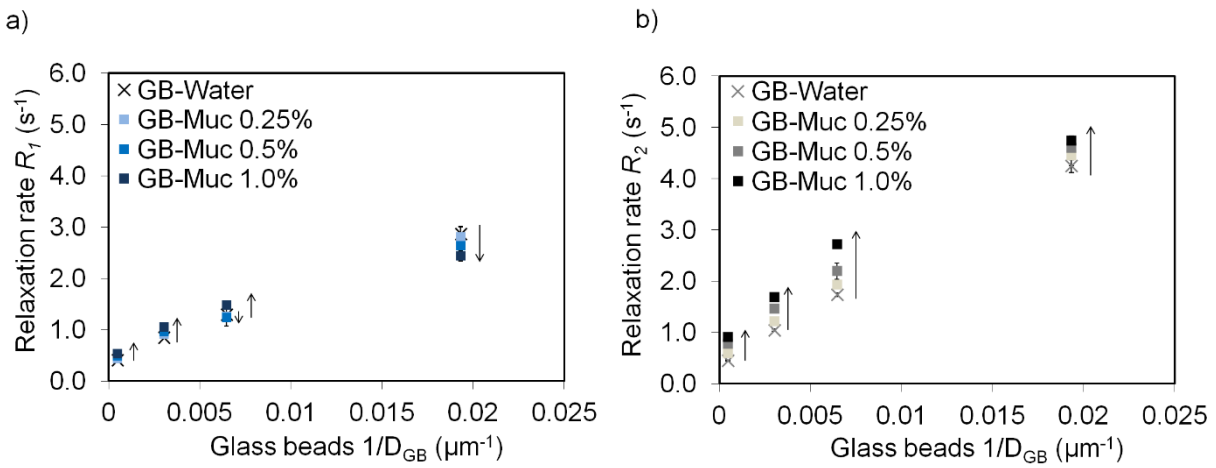

Figure 4: Volumetric pore size distribution of water- and mucilage-filled pores in GB350 (a), and volumetric air bubbles size distribution in GB350 (b) in 2000 mm^3 samples.

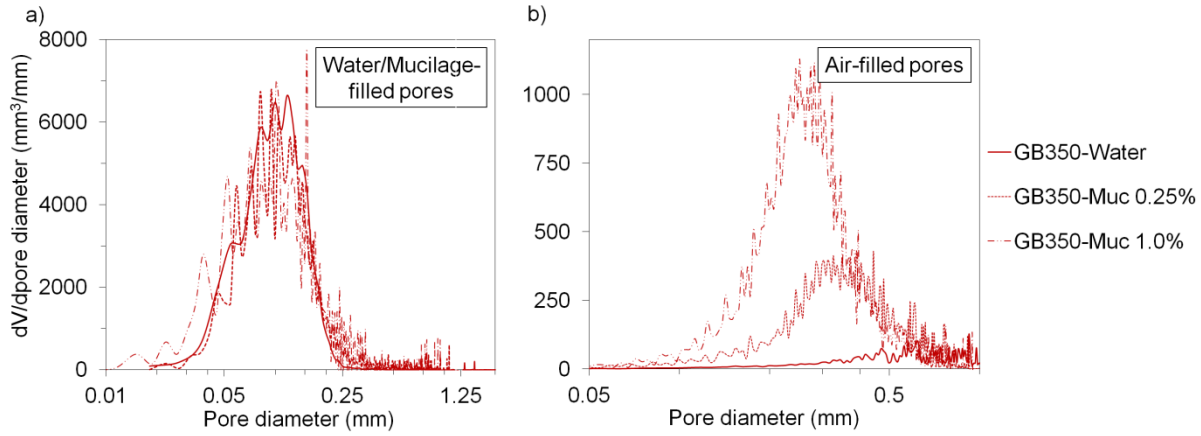

Figure 5: Polymeric network effect G*$_{1\,B}$ (a) and G*$_{2\,B}$ (b) affected by the particle sizes

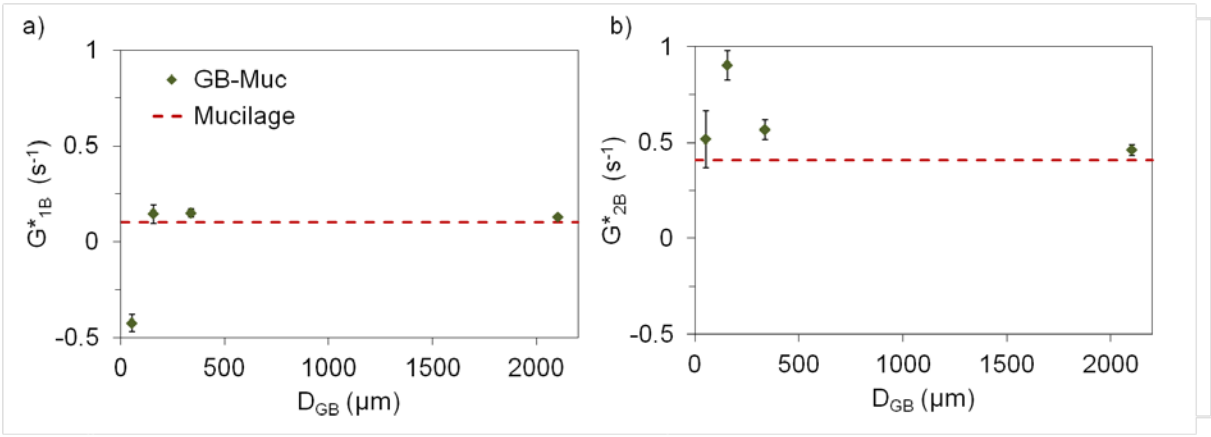

762 **Figure 6:** Schematic representation of the rearrangement of the polymer network according
763 to the porosity.

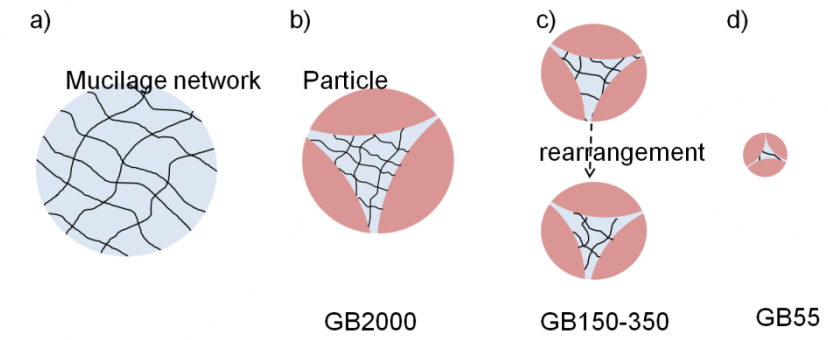

764

765 **Figure 7:** Influence of the mucilage concentration on the surface relaxivity coupled with the
766 pore size proportional factor for the R_2 and the R_1.

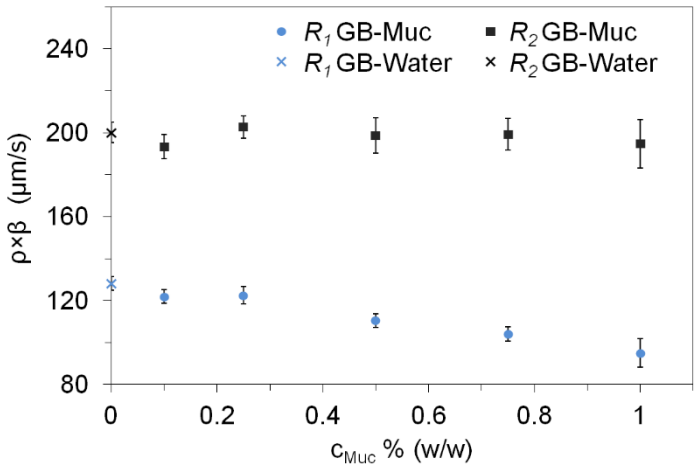

767

768 **Figure 8**: Influence of the mucilage concentration on the longitudinal (a) and transverse (b)
769 bulk relaxation in porous media.

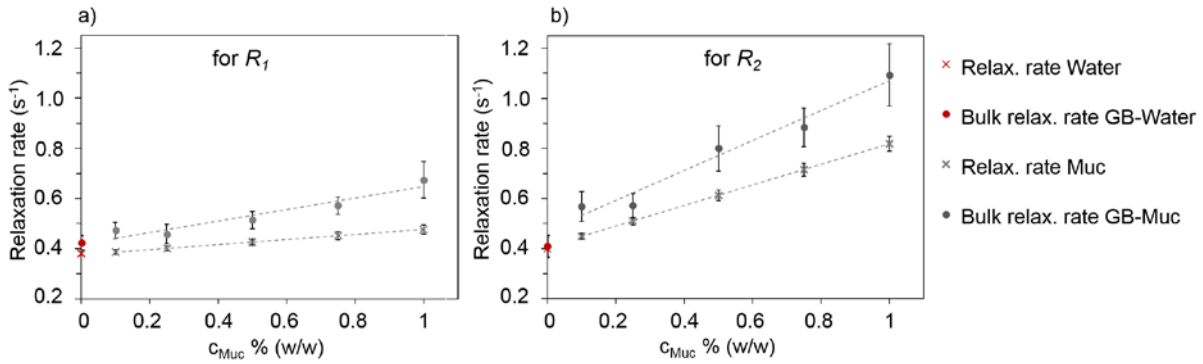

770

7. Tables

Table 1: Particle size and maximal water holding capacity (WHC_{max}) of the glass beads (GB).

	GB2000	GB350	GB150	GB55
Particle size (µm)	2103 ± 29	338 ± 44	157 ± 19	54 ± 10
WHC_{max} % (w/w)	24.5 ± 0.9	25.3 ± 0.8	26.2 ± 0.1	26.2 ± 0.6

Table 2: Statistical values characterizing the linear relationship between the R_1 or the R_2 and the mucilage concentration for all particle sizes.

		GB2000	GB350	GB150	GB55
R_1	pearson R	0.96	0.88	0.59	-0.93
	R^2	0.92	0.78	0.35	0.86
	p-value	3.99E-10	1.29E-05	9.89E-03	2.25E-07
R_2	pearson R	0.97	0.95	0.94	0.68
	R^2	0.94	0.91	0.89	0.47
	p value	4.31E-11	4.44E-08	3.94E-09	3.51E-03

Table 3: Summary of the several gel effects investigated in this paper.

Gel effect	Cause	Translated by	Significant?
Accelerated surface relaxation	Chemico-physical interactions between water protons and polymer	$\rho_{GP}>\rho_{WP}$, but ρ could not be isolated from $\rho \cdot \beta$	no
Accelerated bulk relaxation	Chemico-physical interactions between water protons and polymer	$\frac{1}{T_{1,2\ B/GP}} > \frac{1}{T_{1,2B/WP}}$	yes
Polymer network effect	Polymer organization in the pore space	$G^*_{1,2}$	yes, depends on particle size and mucilage concentration

Spider-web effect	Rigidity of the polymer network in the pore space > in the free polymer	$G^*_{1,2}$ $X_{1,2\ MC} > 0$	yes

778

779